Stability of ⟨100⟩ Dislocations formed in W Collision Cascades

Utkarsh Bhardwaj[a], Andrea E. Sand[b,c], Manoj Warrier[a,d]

[a] *Computational Analysis Division, BARC, Vizag, AP, India-530 012*
[b] *Department of Physics, P.O. Box 43, FI-00014 University of Helsinki, Finland*
[c] *Department of Applied Physics, Aalto University, FI-00076 Aalto, Espoo, FINLAND*
[d] *Homi Bhabha National Institute, Anushaktinagar, Mumbai, Maharashtra, India - 400 094*

Abstract

Experiments and simulations both have verified the presence of ⟨100⟩ dislocations in irradiated W. It is essential to know the properties and behavior of these defects to study the evolution of microstructures at higher scales. We study the thermal stability and transition mechanism of various ⟨100⟩ dislocations formed in a molecular dynamics (MD) database of 230 collision cascades using three different interatomic potentials. The activation energy to transition to more stable ⟨111⟩ dislocations is found for various ⟨100⟩ dislocation defects that transition within the 100 nanosecond time scale that is readily accessible to MD. The stability of ⟨100⟩ dislocations increases with size, but the trend is not strict. The reasons for irregularities are the aspects of internal configuration such as (i) the arrangement of ⟨100⟩ directed crowdions within the defect, (ii) the presence and arrangement of non-⟨100⟩ crowdions on the fringes of the defect. We show the typical pathways of transitions and discuss the sources of instability in the defect configurations. We also discuss the similarities and differences in stability found across different interatomic potentials. Understanding transition mechanisms and internal morphology gives insights into the stability of ⟨100⟩ dislocations, useful in higher scale models such as Kinetic Monte Carlo (KMC).

Keywords: Defect morphology, ⟨100⟩ Dislocations in crystal, Collision cascades, Radiation damage, Molecular dynamics, Stability of Defects

1. Introduction

Molecular dynamics simulations of collision cascades have been used extensively to determine the radiation damage at atomistic scales [1]. The higher scale models of irradiation induced changes in microstructure such as KMC require defect distribution and their properties like diffusion, stability and interaction as inputs [2, 3, 4]. Traditionally, the initial defect distribution input from MD simulation consists of the number of point defects and defect cluster size distribution. These defects have different morphologies which may have different properties for diffusion, stability and interaction. For instance, in W, two kinds of loops are observed: 1/2 $\langle 111 \rangle$ loops which easily glide in one dimension and $\langle 100 \rangle$ loops which glide very slow, and then there are rings that are completely sessile [5, 6, 7]. For simplicity, in various KMC studies, point defects are considered glissile while all other clusters, or clusters above a certain size, are considered sessile [8]. The diffusion affects the extent of interaction between the defects which decides long term microstructural changes. It has been shown that such assumptions about the transport properties has an affect on the predicted damage results of the KMC simulation ([9] and references therein). It is also important to track morphological transitions of defects because transition to a different morphology will change further diffusion and interaction of the defect.

There have been various studies investigating the morphological distribution of defects at different PKA energies in W [7, 6, 10, 11]. The results show that while majority of the SIA defects consist of $\langle 111 \rangle$ dumbbells and dislocation loops, there are also $\langle 100 \rangle$ loops, mixed loops, C15 like rings and their basis structures, and mixed rings and dislocation loops. The $\langle 111 \rangle$ dumbbells and their clusters forming $\langle 111 \rangle$ dislocations are the most stable self-interstitial atom (SIA) defect morphologies in W. These constitute the majority of defects formed in W collision cascade simulations [11, 10, 7]. The prevalence of $\langle 111 \rangle$ dislocations in W simulations is in agreement with the experiments [12, 13, 14]. In addition to the $\langle 111 \rangle$ dislocations, formation of $\langle 100 \rangle$ dislocations on high en-

ergy irradiation of W has also been reported in experiments [14, 13, 12] as well as in MD simulations of collision cascades [11, 10, 6]. The ⟨100⟩ loops inhibit void nucleation and affect the irradiation swelling resistance of the material [15]. Therefore, it becomes important to account for the ⟨100⟩ dislocation loops and their corresponding properties in higher scale modeling of radiation damage in W.

The ⟨100⟩ dislocations have been found in MD simulations carried out with various widely used interatomic potentials [10, 7]. Different potentials show differences in numbers and sizes of different defects morphologies [7]. The PKA energy dependence on morphology of defects has also been studied [10, 6, 7]. The contribution of bigger mixed loop defects increases after around 100 keV while the contributions of single loops specifically ⟨100⟩ loops decrease. However, the maximum size and average size for ⟨100⟩ loop increases with energy for the range 10 keV to 200 keV.

There have been MD studies to explore the stability of specific defects. In [16], stability of three defects of size 2, 8 and 13 produced by displacement cascades in Fe is studied. The three defects studied have different morphologies and sizes. The defects are first isolated so that their stability can be studied without interaction and influence of nearby defects. The defects are annealed at different temperatures and their transition times are noted to find the activation energy for transition (transition energy). Four sample runs are given for size-2 defect at five different temperatures while a single run is given for other two defects at four different temperatures. The maximum duration of a single MD simulation is 1 ns. In [17], transformation of sessile multi-dislocation defects to single 1/2 ⟨111⟩ dislocation is reported by annealing primary damage state of ten 200 keV cascades. Each cascade is annealed at a single temperature of 1500 K for up to 5 ns. Three different interatomic potentials are used to study the effects of interatomic potentials. The estimated transition energy for these defects is reported to be approximately 1.5 eV. As noted in the study, the transition energy is only indicative or qualitative because of the presence of other defects that affect stress fields and may interact with the defect being

studied.

The shape and internal configuration of ⟨100⟩ loops has also been studied. Eyre and Bullough in [18] show that the experimental findings of rectilinear shape of ⟨100⟩ loops in bcc metals is due to lower elastic energy of rectilinear shape when compared to circular. The ⟨100⟩ loops maintain rectilinear shape as the size grows while bigger ⟨111⟩ loops are circular. The study also shows that the rectilinear loops will tend to be square i.e. the ratio of length to breadth (aspect ratio) of the rectilinear shape will tend to be lower. Setyawan et el. in [10] show that the shape of ⟨100⟩ loops observed in MD simulations of collision cascades in W are parallelogram (or a rhombus). It has been shown for ⟨111⟩ dislocations in Fe that the energy density of the crowdions in the center of the defect is lower than that on the interface [19]. This has also been observed and analyzed for both ⟨111⟩ and ⟨100⟩ dislocations in W [6]. The study also shows that the ⟨100⟩ dislocation loops found in MD simulations of collision cascades in W have a ⟨100⟩ bunch of dumbbells surrounded by non-⟨100⟩ dumbbells on the fringes.

This work examines the thermal stability and transition mechanism of ⟨100⟩ dislocations of varying sizes and configurations formed in W collision cascade simulations using MD. We examine 34 ⟨100⟩ dislocations in a database of 230 collision cascades carried out using three widely used interatomic potentials. We isolate the defects and then carry out annealing MD simulations. To calculate transition energy of a defect, we carry out 16 runs for maximum of 10 ns at 12 different temperatures which amounts to 192 runs to estimate the transition energy of a single defect. We carry out a systematic study with size and discuss the relationship between size and transition energy of ⟨100⟩ dislocations. The activation energy for transition to ⟨111⟩ dislocations of various medium-size ⟨100⟩ dislocations, including clusters of 6 to 24 self interstitial atoms (SIAs) is found to be in the range of 0.1 eV to 3.2 eV. We show that the transition energy increases with an increase in defect size. However, the trend is neither continuous nor regular. To understand the reason behind irregularities, we analyze the internal configuration of defects using the SaVi [6] algorithm. We

show that the differences in transition energy of same sized defects is due to the differences in their internal configuration while defects with different sizes also have similar stability if the arrangement of ⟨100⟩ dumbbells is the same. We further understand the relationship of internal configuration, defect size and defect stability by showing the typical transition pathways that highlight the sources of instability. We also discuss the similarities and differences in stability of ⟨100⟩ dislocations appearing in the different interatomic potentials.

2. Methods

2.1. MD simulation

The ⟨100⟩ dislocations explored consist of 34 defects formed in 230 collision cascades. The procedure used for the collision cascade simulations and the identification of defect morphologies is discussed in detail in [6, 7]. The database consists of collision cascades using three interatomic potentials: Finnis-Sinclair potential [20] as modified by Juslin et al. (JW) [21], the potential by Derlet et al. [22] with the repulsive part fitted by Björkas et al. [23] (DND-BN), and the potential by Marinica et al. [24], stiffened for cascade simulations by Sand et al. (M-S) [25]. Collision cascades from multiple potentials help in analysing the effect of choice of potential on the stability of ⟨100⟩ dislocations loops. We selected these three potentials owing to the large collision cascade database that is available with us for these three potentials.

The stability analysis and transition energy calculation is carried out on the simulation results of several annealing MD simulations. The simulations were performed for each ⟨100⟩ dislocation loop in isolation at different temperatures. We first extract the desired defect along with five extra unit cells around it from the simulation box of the collision cascade. We then add more unit cells of W on each side of the extracted volume to form a simulation box of at least five times the extracted number of unit cells in each direction to take care of finite size effects. The Large-scale Atomic Molecular Massively Parallel Simulator (LAMMPS) [26] code is used to carry out MD simulations to relax the system using an NPT ensemble at 300 K with periodic boundary conditions (PBC) and

zero pressure. This relaxation step is essential given that we have placed the defects and their nearby unit-cells into a new crystal. We analyse the dislocation after the relaxation for any change in structure or inconsistency.

For each relaxed system we carry out a temperature ramping simulation from 300K to 2000K. The temperature at which the defect transitions to $\langle 111 \rangle$ dislocation (T_r) in a ramping simulation is noted. We calculate 12 temperatures (T_1 to T_{12}) around T_r with a difference of 25K i.e. $(T_2 - T_1) = (T_3 - T_2) = ... = (T_{12} - T_{11}) = 25$K and $T_7 = T_r$. After that, sixteen different NPT runs are carried out at each of these temperatures with different random number seeds for initializing the temperature. Periodic boundaries are set at zero pressure. These simulations are stopped either at 50 ns or if the defect transitions to $\langle 111 \rangle$ dislocation. For cases where most of the sample runs transition while a few do not transition at a certain temperature, the non-transitioning simulations are extended for 100 ns. The temperatures where transitions occur are included for the transition energy calculation. We do not calculate the transition energy of a defect if it does not transition for the complete 100 ns run even at a high temperature of 2000 K. We use an output frequency of 2 ps for checking transitioning and configuration changes.

For transition energy calculation, the temperature (T) dependence of time for transition (τ) is taken to be described by an Arrhenius expression:

$$\tau = \tau_o exp(E_t/k_b T) \tag{1}$$

where τ_0 is a pre-exponential factor, E_t is the activation energy for transition to $\langle 111 \rangle$ loop and k_b is the Boltzmann constant. A linear regression fit for the equation is found for different runs of each defect. Figure 1 shows a sample fit for a defect of size 11. The plot shows the time of transition of the $\langle 100 \rangle$ loop to $\langle 111 \rangle$ loop for different runs at eleven different temperatures. Out of the total twelve temperatures considered initially, for the lowest temperature a few of the runs did not transition within the 100 ns time limit. For this reason only eleven temperatures are shown in the plot. The temperature range is from 550K to

800 K with an interval of 25K. At each temperature there are sixteen different runs having different transition times. All these data-points from the eleven temperatures are included for the transition energy calculation. The transition time is governed by a Poisson distribution which results in a spread of transition times at each temperature. Moreover, different transition pathways and changes in configurations (as discussed in Section 3.1 and Section 3.3) further add to the variation in the transition times of different runs at a specific temperature.

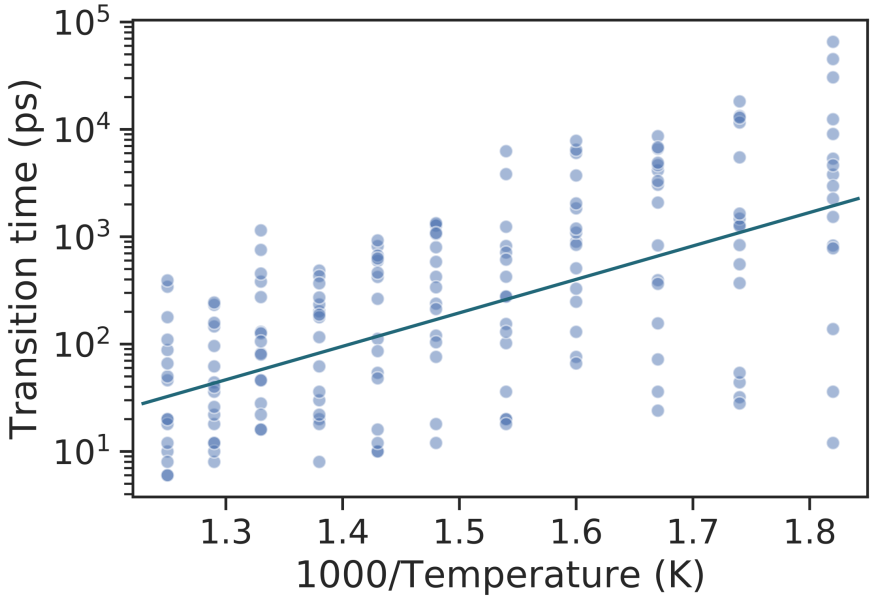

Figure 1: The transition time in various sample simulation runs of a size 11 ⟨100⟩ dislocation loop as a function of annealing temperature. The slope of the linear regression fit is proportional to the transition energy E_t as given in Equation (1).

2.2. Analysis of MD simulation

We track morphological changes using the SaVi algorithm [6] and use CSaransh [27] to visualize the defects. In addition to identifying when the morphological transition occurs, SaVi also outputs various parameters such as the number of dumbbells/crowdions in specific orientations at each step and the number of neighbors of each dumbbell/crowdion. These parameters define the internal morphology and help understand the relationship between stability and internal

configuration.

SaVi algorithm uses computational geometry and graph data-structure to find the various morphological components of a defect and identify the overall morphology based on the components. The algorithm finds lines across all the dumbbells and crowdions. The direction of the lines decide the orientation of a dumbbell or a crowdion. The lines that share a specific angle and distance form a morphological component. For instance, a dislocation is formed by lines that are approximately parallel to each other, while a hexagonal ring is formed by lines that have 60 degree angle. The direction of the Burgers vector for a dislocation loop is found by the orientation of the constituent lines while the magnitude is decided by the number of net defects in each line. The algorithm involves several details that make it robust to noise such as finding cycles for asserting rings. The algorithm can be used to find if a dumbbell is at the center of the defect or on the surface by counting its number of nearest neighbouring parallel lines.

2.3. Naming Internal Configuration

The arrangement of dumbbells and crowdions in a dislocation decides the energy density and stability[19, 18]. This forms the basis of examining relationship between stability and internal configuration. For the discussions of internal configurations, it is important to express it in a way that conveys the shape of the defect especially the factors that are observed to affect the stability.

The $\langle 100 \rangle$ dumbbells in a $\langle 100 \rangle$ loop arrange in rectilinear form [18]. More specifically, in a parallelogram or rhombus shape [10] along with a few residual dumbbells outside the full parallelogram [6]. We utilize the length, breadth and residual number of $\langle 100 \rangle$ dumbbells to name the configuration of $\langle 100 \rangle$ dumbbells. The naming scheme also signifies the degree to which dumbbells are packed at the center in a configuration and can help in understanding stability differences for same sized defects. The scheme used to name a configuration of size s is as follows:

$$s = n + m \tag{2}$$

$$n = (l \times b + r) \tag{3}$$

where, n is the number of $\langle 100 \rangle$ dumbbells while m is the number of non-$\langle 100 \rangle$ dumbbells on the fringes. The configuration of $\langle 100 \rangle$ dumbbells is further divided into l, b and r where l and b are the length and breadth of the number of completely filled rows and columns (sides of parallelogram) formed by the $\langle 100 \rangle$ dumbbells. r is the remaining or residual number of $\langle 100 \rangle$ dumbbells. The values of l and b are to be chosen such that the residual r has a minimum value. Figure 2 shows a schematic representation of a few defect configurations and their corresponding parameters for naming.

We say that two defect configurations are different if any of the values of l, b, r or m are different. Another feature that we will note in a defect configuration is the ratio of l and b, which we refer to the aspect ratio of the $\langle 100 \rangle$ component. This ratio together with number of residual dumbbells gives an idea about the number of dumbbells that will be on the edges. As shown in [18], the $\langle 100 \rangle$ loops tend to have lower aspect ratio.

In place of current naming scheme, one can find the number of $\langle 100 \rangle$ neighbors for each $\langle 100 \rangle$ dumbbell and use this neighbour count for comparing the stability of defects where sizes are same. A dumbbell in the center would have four $\langle 100 \rangle$ nearest neighbors while the one on the interface will have less than four. This scheme might be more appropriate for quantitative comparison or for loops that are more often circular than rectilinear. One drawback of the neighbor count based scheme is that it does not give a picture of the arrangement for qualitative discussion. In Section 3.3, we will discuss the relationship of the stability of a configuration with the different factors of the notation that we have used.

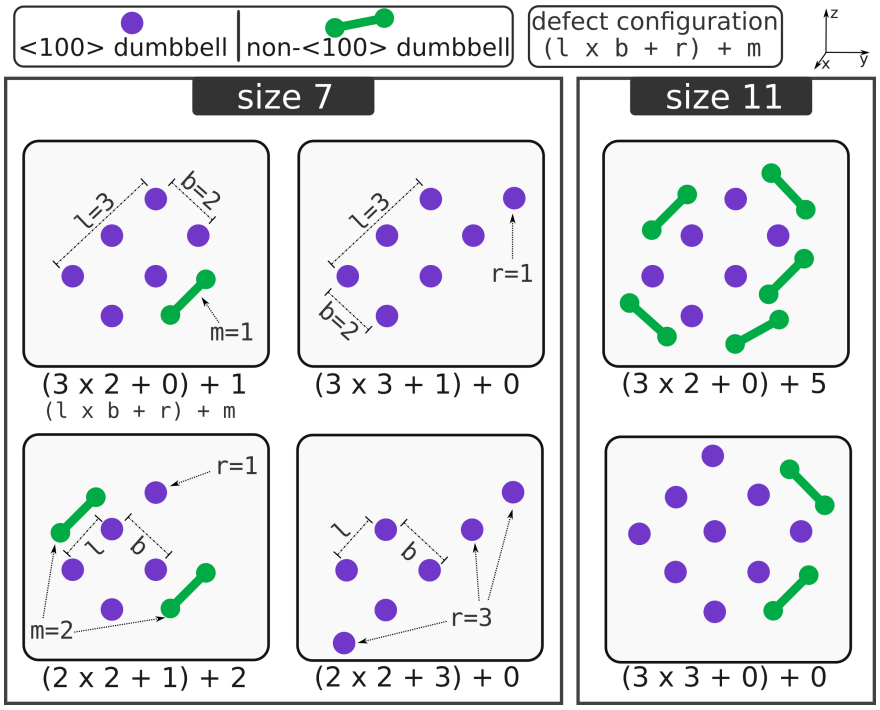

Figure 2: The schematic shows naming parameters for four configurations of size-7 and two configurations of size-11 ⟨100⟩ dislocations. The naming helps in expressing the arrangement of dumbbells in a ⟨100⟩ dislocation. The parameters like l, b, their ratio also give an idea of the number of dumbbells in the center of the defect and on the edges which has an affect on the stability of the defect. The legend at the top shows colors and symbols for dumbbell orientation, parameters for the expressions written below each defect and axis orientation for the plot.

3. Results

The database of ⟨100⟩ edge dislocations contains 34 defects found in a database of 230 collision cascades simulated with the three different potentials at PKA energies ranging from 5 keV to 200 keV. The distribution of different morphologies and defect size distribution for each morphology for a subset of the database has been earlier shown in [7, 6]. The fraction of defects forming ⟨100⟩ loops reduce after around 100 keV energy but the maximum possible size of ⟨100⟩ loop increases with energy. There is no dependence of internal configuration on PKA energy. All the three potentials predict damage containing ⟨100⟩ dislocations, with almost all the defects having a size between 4 and 50

(the DND-BN potential has an outlier defect of size 147). The size of a defect refers to the number of SIAs in the defect. Figure 3 shows the frequency of different sizes of defects present in the database for each of the potentials. Sizes 29 or bigger are grouped because there are no transitions observed within MD timescales for defects of sizes 29 onward for all the three potentials.

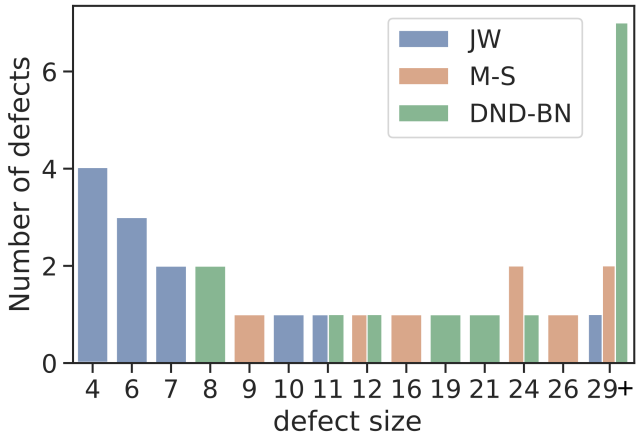

Figure 3: The number of ⟨100⟩ defects for all the defect sizes present in the database for each of the potentials. The values for each potential are shown separately with different colors. Defect size implies the number of SIAs in the defect.

Out of the total 34 ⟨100⟩ dislocations in the database, the transition energies for 17 defects were calculated. From the remaining 17 defects, 13 large defects do not transition during MD simulations of 100 ns at 2000K temperature, whereas four defects of size four transition to ⟨111⟩ during the one nanosecond relaxation run at room temperature. Figure 4 shows the different configurations of the 17 defects that transition to ⟨111⟩ dislocation. A single defect can switch to different arrangements while being in ⟨100⟩ dislocation morphology within a single simulation. The figure also lists other prevalent configurations for the defects having multiple stable configurations.

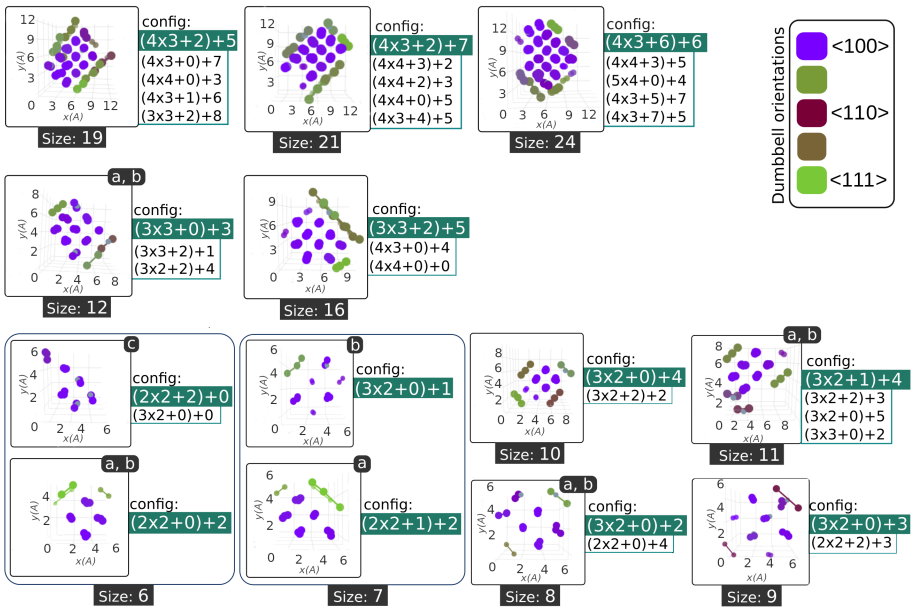

Figure 4: Defects that show transition within the maximum MD simulation time of 100 ns at a maximum temperature of 2000 K. A single configuration is shown for each defect. Other prevalent configurations are listed for the defects that change configuration. Different defects in same size are marked as a, b and c. A single plot is shown for multiple defects if the defects have exactly the same configuration such as for size 6 there are two defects with exactly same configuration which are shown with a single plot marked with a and b. The axes for each defect are shown to give an idea of the defect dimensions.

3.1. Configuration Dynamics and Transition Mechanism

We find the changes in configurations and transition mechanisms in the simulations by tracing the movements and rotations of dumbbells that are in the center and on the edges. Although in some cases the configuration changes can be too quick and non-recurring, most of the times the transition pathways and configuration changes fall clearly in one of the two categories shown in Figure 5. These two paths are representative of the reoccurring patterns that we observe for all the transitioning defects. The figure traces the significant changes in defect configurations for two separate runs of a size-12 defect as it transitions to $\langle 111 \rangle$ dislocation. The initial configuration of the defect is $(3 \times 3 + 2) + 1$ (shown left of the center in Figure 5).

Path-A is the preferred path of configuration changes and transition when $r = 0$. In Figure 5 path-A starts when the defect transitions from initial config-

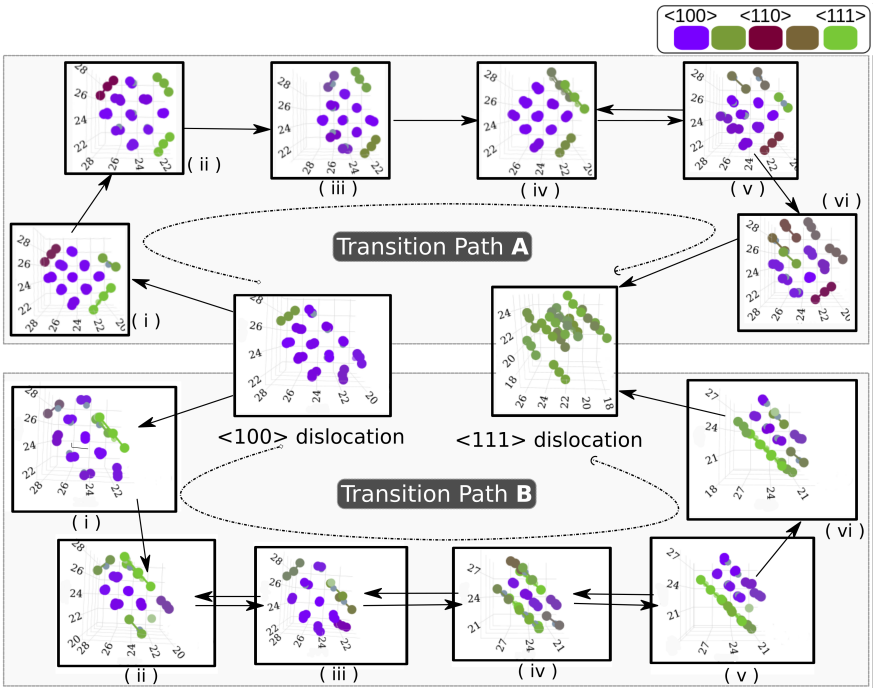

Figure 5: Two typical dynamics of dumbbell rotations and pathways for transition of ⟨100⟩ dislocations to ⟨111⟩ dislocations. Path-A is common in configurations that have no residual ⟨100⟩ dumbbells forming a ⟨100⟩ configuration with complete parallelogram/rhombus. The arrows show the time evolution of configurations. Different changes in configurations are shown as the size 12 defect transitions to ⟨111⟩ dislocation. For both paths, the rotation of ⟨100⟩ dumbbells is initiated at edges.

uration to $3 \times 3 + 0$ configuration. The non-⟨100⟩ dumbbells move around the fringes from one side to the other while the ⟨100⟩ dumbbells remain stable in the same configuration. This movement can result in a climb of the dislocation loop, which is observed to occur rarely. However, glide in these dislocations is much more common. As the non-⟨100⟩ dumbbells move around, they may meet and cluster, making the defect slightly unstable, inducing rotation in adjacent ⟨100⟩ dumbbells to non-⟨100⟩. In our example, this is shown by Figure 5 (i) to (v) of Path A. The rotation of the adjacent dumbbells in the ⟨100⟩ bunch may go back and forth for some time. At some point, a good majority of the dumbbells in the main bunch rotate, resulting in the transition to highly glissile ⟨111⟩ dislocation. In a bigger ⟨100⟩ dislocation, the number of ⟨100⟩ dumbbells

is more, and it becomes difficult to reach an instance when a majority of main $\langle 100 \rangle$ dumbbells are in the non-$\langle 100 \rangle$ direction. A bigger defect may either stay as a multi-component mixed loop or may keep looping between stages similar to (iv) and (v), thus taking longer to eventually transition.

Path-B is typical when $r > 0$ or multiple non-$\langle 100 \rangle$ dumbbells are distributed unevenly around the $\langle 100 \rangle$ component. The exact arrangement of the $\langle 100 \rangle$ dumbbells keeps changing very often as the $\langle 100 \rangle$ dumbbells on the edges keep rotating from $\langle 100 \rangle$ to non-$\langle 100 \rangle$ as shown in Figure 5 (ii) to (v). At a certain moment, the rotation may travel from the edge towards the center of the dislocation. If a majority of dumbbells get rotated away from $\langle 100 \rangle$, the dislocation rather than coming back to $\langle 100 \rangle$ sways entirely to $\langle 111 \rangle$ dislocation (Figure 5 (vi)). Again, if the value of n is greater with more $\langle 100 \rangle$ dumbbells packed inside, it is more likely for the rotating non-$\langle 100 \rangle$ dumbbells to sway back rather than the disturbance penetrating deep resulting in the rotation of all $\langle 100 \rangle$ dumbbells.

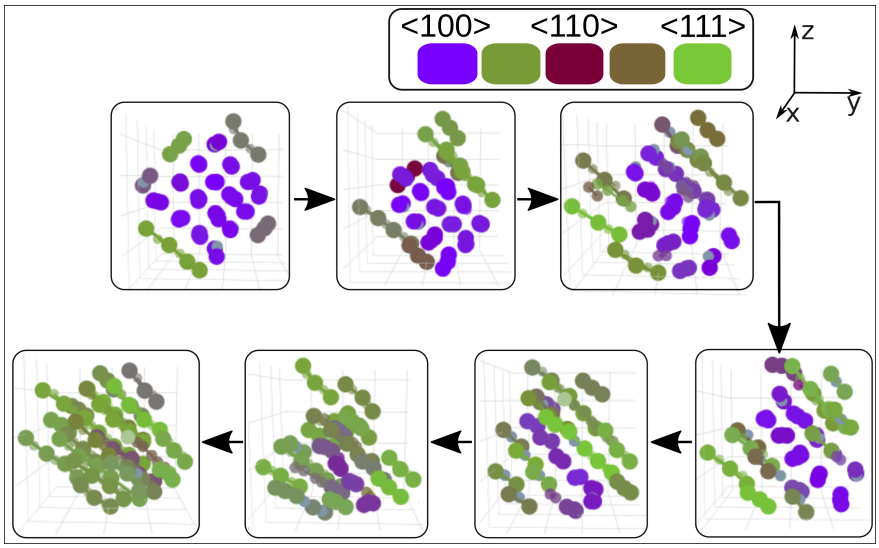

Figure 6: The transition pathway of a size 21 defect showing rotation of dumbbells from edges to center. As the initial configuration is a full parallelogram ($r = 0$), path-A is taken. The arrows show the time evolution of configurations. The configurations in second row change relatively quickly.

It must be noted that at any time the further dynamics of defect configurations may change from one path to another if the defect configuration changes in such a way. For instance, if an incomplete parallelogram ($r > 0$) transitions to a smaller but complete parallelogram ($r = 0$) then the pattern of further configuration changes will be based on path-A.

For both paths, the transition starts from the edges and moves towards the central part. Figure 6 shows transition of a size twenty-one defect. The rotation of dumbbells can be clearly seen to be initiated at the edges and then moving towards the center. For a bigger defect the half rotated configurations in first row are more stable. The defect may stay as a mixed loop for longer time. The configuration then may sway back to $\langle 100 \rangle$ again or may trickle down to $\langle 111 \rangle$ loop as in the second row of the Figure 6. The final transition stages are quick and same in both the paths.The relative instability of dumbbells/crowdions at the edges compared to central ones can be understood by their higher energy density as shown in [19, 6]. This difference in stability is also observed in our further examination of the relationship between internal morphology and stability in Section 3.3.

3.2. Size dependence of Transition energy

Figure 7 shows the transition energy of various $\langle 100 \rangle$ dislocations for transitioning to $\langle 111 \rangle$ dislocations as a function of defect size. The configuration of these defects are shown in Figure 4. In case there are multiple defects of the same size, the defects in Figure 4 are labeled by alphabets (a), (b) and so on, starting from defect with lower transition energy in Figure 7. The overall trend in Figure 7 shows an increase in defect stability with an increase in size.

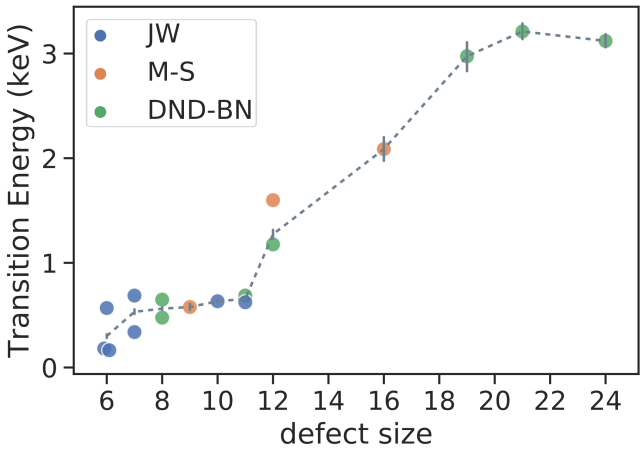

Figure 7: Transition energy for various defects. Different colors are used for different potentials. The transition energy increases with defect size. The error bars represent the 95% confidence interval for the transition energy fit.

The majority of ⟨100⟩ dislocation loops that get formed in a collision cascade are of the size ranges that will transition to ⟨111⟩ dislocation loops at elevated temperatures. This is in agreement with the experimental findings that the number of ⟨100⟩ loops reduce at elevated temperatures [28].

The transition energy does not increase linearly with size but rather in steps. It remains comparable for a few similar sizes and then increases sharply. For example, in Figure 7 we see that sizes 7 to 11 have comparable transition energy, and then for size 12, it increases sharply. Again, the transition energy values are similar for sizes 19, 21, and 24, whereas size 29 is too stable to transition within the MD simulation time limits, even at a temperature of 2000 K. We also observe that defects of the same size may have different transition energy. For example, out of the three defects of size six, two have similar transition energy, whereas the third has higher transition energy (Figure 7) though all three defects are created in collision cascades using the JW interatomic potential. The internal morphology as discussed in next subsection reveals the reason behind these observations.

3.3. Internal morphology and stability

3.3.1. Transition energy of different configurations for the same size defects

There are more than one defects for the sizes 6, 7, 8, 11 and 12. The transition energy of two defects with size 6 (labeled as (a) and (b) in Figure 4) is same while another defect (labeled as (c)) has a higher value of transition energy. Figure 4 shows the difference in configuration of (a), (b) and (c). While (a) and (b) have $n = 4$ (number of $\langle 100 \rangle$ dumbbells), (c) has $n = 6$. The difference in transition energy and configuration can also be noted for size-7 (a) and (b), with $n = 5$ and $n = 6$, respectively. For the two defects of size 8 and size 11, the transition energy and configurations remain the same. We see that there is a direct correlation between the number of dumbbells in the $\langle 100 \rangle$ orientation (n) and transition energy for the same sized defect. For size 12, the two defects have more or less similar configurations, however the transition energy is slightly different. This might be because the defect with higher energy belongs to the M-S potential, that behaves differently from the other two potentials as discussed in Section 3.4.

A defect can transition from one configuration to another as it thermally vibrates. The two size-8 defects have initial configuration of $(2 \times 2 + 0) + 4$ and in most of the sample simulations they transition to $(3 \times 2 + 2) + 0$ configuration before finally transitioning to a $\langle 111 \rangle$ dislocation. Figure 8 shows the transition time as a function of temperature for all the different sample runs of the defect. We see that the transition time of the samples that remain in 2×2 configuration is generally lower than the samples where the configuration changes to a 3×2 configuration in the beginning of the simulation. Once the defect transitions to a 3×2 configuration it takes longer to transition while in 2×2 configuration it never stays as $\langle 100 \rangle$ loop for long. In the figure, We see that the transition time of the samples that remain 2×2 configuration is generally lower than the samples where the configuration changes to 3×2 configuration in the beginning of the simulation. The 3×2 configuration is present in more samples and is also a more stable configuration.

The bigger defects have a lot more possible configurations that they can

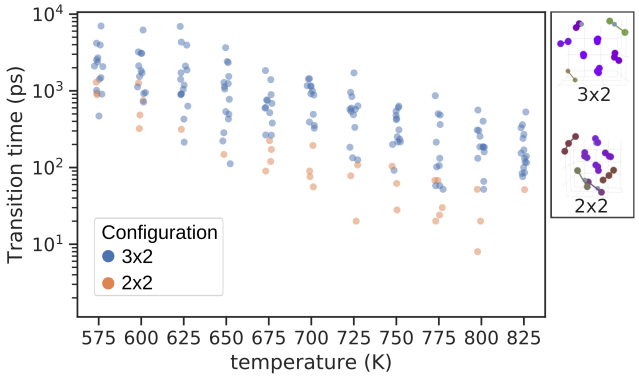

Figure 8: Time to transition to ⟨111⟩ dislocation for different sample runs at various temperatures for a size 8 defect (Figure 4). The transition time for the initial 2×2 configuration is almost always shorter. From the initial 2×2 configuration, the defect either changes to a more stable 3×2 configuration or transitions to ⟨111⟩ dislocation quickly.

transition between. However, there are certain configurations that are very stable and remain same for a long duration. We observe that the configurations with $r = 0$ and $m = 0$ are not found in our dataset of 230 cascades. The defect with size 6 and size 16 both have a few runs that transition from a different initial configuration to a configuration with $r = 0$ and $m = 0$, 3×2 and 4×4, respectively. These configurations are observed to be more stable but transition to these occurs rarely.

3.3.2. Similar transition energy of different sizes

All of the defects in the size range of 8 to 11 have $l \times b = 3 \times 2$ (while r varies from 0 to 1 and m ranges from 2 to 4). The transition energy of all these defects are similar. For size-7, the transition energy of the defect with $(2 \times 2 + 1)$ configuration of ⟨100⟩ dumbbells is lower, while the one with $(3 \times 2 + 0)$ has slightly higher transition energy compared to other 3×2 configurations. A jump in the value of transition energy is accompanied with configurational change at size 12. The stable configuration of ⟨100⟩ dumbbells for size 12 defects is $l \times b = 3 \times 3$. For size 16 defect the transition energy as well as value of n increases with possible configurations of $3 \times 3 + 2$, $4 \times 3 + 0$ or $4 \times 4 + 0$. The transition energy of sizes 19, 21 and 24 is higher than others but remains similar to each other. This agrees with the similarity in their configuration

having $l \times b = 4 \times 3$.

The similarity of the configuration of $\langle 100 \rangle$ component for a wide range of sizes can be seen as the preference for addition of non-$\langle 100 \rangle$ dumbbells on the fringes rather than having residual $\langle 100 \rangle$ dumbbells or changing to a lower aspect ratio configuration. We note that the configurations with higher aspect ratio are preferred over the ones with lower aspect ratio, e.g. we find 4×3 but not 6×2 for 12 $\langle 100 \rangle$ dumbbells. Similarly, the configurations like 4×2 or 5×2 are never observed, rather the extra dumbbells with increase in size get added on the fringes of 3×2 as non-$\langle 100 \rangle$ dumbbells until the size reaches to a point where 3×3 is possible with a few extra non-$\langle 100 \rangle$ dumbbells. A low aspect ratio arrangement or addition of residual $\langle 100 \rangle$ dumbbells increases the fraction of $\langle 100 \rangle$ dumbbells on the edges of the defect. The residual $\langle 100 \rangle$ dumbbells on the edges will have a high energy density which explains the preference of configurations towards non-$\langle 100 \rangle$ dumbbells over residual $\langle 100 \rangle$ dumbbells. [18] shows similar result using elastic energy comparison of rectilinear and circular $\langle 100 \rangle$ loops. It shows that the $\langle 100 \rangle$ loops grow from all the four sides keeping the shape rectilinear and square (or low aspect ratio) even for bigger sizes as opposed to $\langle 111 \rangle$ loops that change to circular arrangement as the size increases.

The tendency to reduce the fraction of dumbbells on edges explains the similarity of configurations for very similar sized defects where bigger stable configuration is not possible. However, it does not explain that the defect sizes that can have bigger stable configurations still stick to the smaller configuration with more of the extra non-$\langle 100 \rangle$ dumbbells on the edges. This might be due to higher formation energy required for a bigger $\langle 100 \rangle$ core. For instance, a size 8 defect can not attain 3×3 configuration (of 9 $\langle 100 \rangle$ dumbbells) and remains in 3×2 configuration, but size-10 or size-11 defect can have 3×3 configuration with a few non-$\langle 100 \rangle$ dumbbells still left. However, we only observe 3×2 configurations for these sizes too. Similarly, bigger sized defects such as size 19, 21, 24 do not have configurations that would maximize the number of $\langle 100 \rangle$ dumbbells.

3.4. Interatomic Potential and Stability

The transition energies of ⟨100⟩ dislocations of different sizes show similar values and trends for all three potentials. However, there are a few differences, especially in the M-S potential.

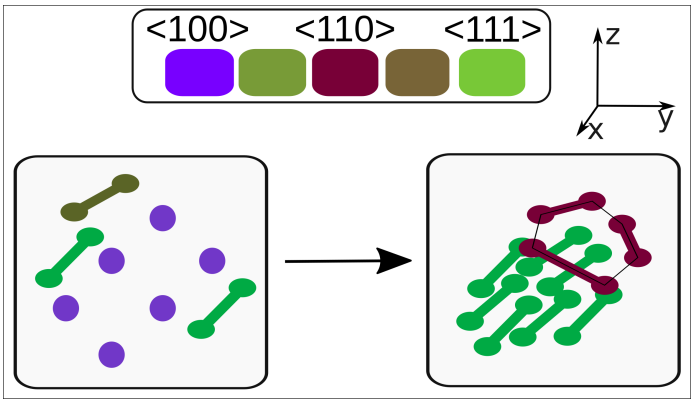

Figure 9: The ⟨100⟩ dislocation with an initial configuration of 3x2 (left) and a total size nine occasionally transitions to a mixed hexagonal ring (composed of ⟨110⟩ dumbbells) + ⟨111⟩ dislocation morphology (right). The mixed morphology defect is sessile and very stable. The dumbbells are colored according to their orientation, with a color map shown in the legend.

The size-9 defect in M-S potential sometimes transitions to a mixed morphology defect having a component of ⟨111⟩ dislocation and a hexagonal ring as shown in Figure 9. Although the transition to mixed morphology is rare, it is significant because once formed, this mixed configuration is very stable in M-S and does not transition even at very high temperatures like 2000 K. Also, such ring-like defects are formed relatively more often in collision cascades with M-S potential than with the other two potentials [7]. The M-S potential has been fitted using liquid configurations in addition to perfect crystal and point defects. For this reason, it might be more accurate about the stability of rings in W.

Defects of size 19 onward in M-S do not transition within the limits of our simulations, while for DND-BN, the defects up to size 24 transition. The two defects with size 12 have same configurations but different interatomic potentials. The one that belongs to M-S potential has higher transition energy than

the other one that belongs to the DND-BN potential (Figure 4). In [17], it has been shown that the big multi-component dislocations are highly stable in M-S, while it is not the case with other potentials that they use. It has also been shown that the M-S potential stabilizes ⟨100⟩ dislocation loops over 1/2 ⟨111⟩ [29]. Our observation also indicate that the transition energy for ⟨100⟩ dislocations is higher in the M-S potential compared to the other two potentials especially for bigger sizes in our dataset.

4. Conclusion

We show that the activation energy of a ⟨100⟩ dislocation to transition to ⟨111⟩ dislocation depends on the size and internal configuration. The bigger ⟨100⟩ dislocations are stable. Several defects formed in collision cascades are of small size and might transition to ⟨111⟩ dislocations due to their low transition energy. This is in agreement with the results from experiments that show that at elevated temperatures the number of ⟨100⟩ loops reduce. We explored the internal configurations of different ⟨100⟩ dislocations to understand the relationship between defect size, internal configuration and factors that affect the transition energy that are not clear when considering only the size. We observe that many similar sized defects have similar configuration of ⟨100⟩ component which results in comparable transition energy for a wide band of sizes. We show that various comparable sizes that have same ⟨100⟩ configurations have same transition energy while two same sized defects with different configurations have different transition energy.

The similarity of ⟨100⟩ configurations for similar sized dislocations is due to the preference of ⟨100⟩ dislocations for having non-⟨100⟩ dumbbells on the fringes rather than having residual ⟨100⟩ dumbbells on the corners or having a low aspect ratio configuration with elongated spread of ⟨100⟩ dumbbells. A high aspect ratio puts less dumbbells on the interface. The dumbbells in the center are known to have lower energy density than the ones on the edges. Our results also agree with analytical results that show that the ⟨100⟩ loops prefer square rectilinear shapes [18]. No noticeable affect on the transition energy is observed

due to small changes in the fraction of non-⟨100⟩ dumbbells. The configurational dynamics show that the non-⟨100⟩ dumbbells on the fringes move around the defect. The transition occurs by rotation of dumbbells from ⟨100⟩ to ⟨111⟩ starting from the edges of the ⟨100⟩ component of the dislocation where energy density is high. If a configuration has residual ⟨100⟩ dumbbells on the edges or corner then the dumbbells on the edges with high energy density keep rotating back and forth from ⟨100⟩ to non-⟨100⟩ very often. If there are no residual ⟨100⟩ dumbbells and the ⟨100⟩ dumbbells form complete parallelogram/rhombus, the ⟨100⟩ dumbbell arrangement remains more stable. The movement of non-⟨100⟩ dumbbells on the fringes can also induce instability in a defect. The internal configurations found and the transition pathways observed have good agreement across the potentials. However, the transition energy seems to be slightly higher for the M-S potential especially for bigger size defects. This is in agreement with other ab-initio and simulation results that show that the M-S potential stabilizes ⟨100⟩ loops more than the ⟨111⟩ loops

The understanding of the correspondence of defect sizes with configurations and trends of transition energy with configuration can be used to approximate the transition energy values for input to higher scale models like KMC. It is difficult to say how well the trends of transition energy with size will generalize to very big ⟨100⟩ dislocations. A bigger data-set might enable quantification of various relationships between different factors such as transition energy, size and configurations. This study can also guide a similar stability study for mixed dislocations morphology (having both ⟨100⟩ and ⟨111⟩ dislocations) which constitute a bigger proportion of defects formed in high energy W collision cascades. Other crucial properties for higher scale models include diffusion of ⟨100⟩ dislocations and their interactions with other defects. The systematic studies of the defect properties for each prominent morphology can help in higher scale modeling of the evolution of microstructure after irradiation and for designing materials with desired properties. Other methods such as NEB and ab-initio studies can further supplement the properties found using dynamic MD simulations. A KMC study that accounts for transition energy, migration energy and

interactions of different morphologies and sizes accurately can be used to match experimental results quantitatively. The presented transition energy results and insights into stability of ⟨100⟩ loops form part of the input to such a higher scale study.

Acknowledgments

We would like to thank the supercomputing department of the Indian Plasma Research Institute for providing the high performance computing facility for carrying out the simulations.

References

[1] R. E. Stoller, Primary radiation damage formation, in: R. J. M. Konings (Ed.), Comprehensive Nuclear Materials, Elsevier, 2012.

[2] B. D. Wirth, M. J. Catural, T. D. de la Rubia, T. Khraishi, H. Zbib, Mechanical property degradation in irradiated materials: A multiscale modeling approach, Nuclear Instruments and Methods in Physics Research B (180) (2001) 23–31.

[3] C. S. Becquart, A. Barbu, J. L. Bocquet, M. J. C. et al., Modeling the long-term evolution of the primary damage in ferritic alloys using coarse-grained methods, Jnl. Nucl. Mater. 406 (2010) 39–54.

[4] R. E. Stoller, L. K. Mansur, An assessment of radiation damage models and methods, ORNL report ORNL/TM-2005/506 (2005).

[5] L. Liu, N. Gao, Y. Chen, R. Qiu, W. Hu, F. Gao, H. Deng, Formation mechanism of ⟨111⟩ interstitial dislocation loops from irradiation-induced c15 clusters in tungsten, Phys. Rev. Materials 5 (2021) 093605. doi:10.1103/PhysRevMaterials.5.093605.
URL https://link.aps.org/doi/10.1103/PhysRevMaterials.5.093605

[6] U. Bhardwaj, A. E. Sand, M. Warrier, Graph theory based approach to characterize self interstitial defect morphology, Computational Materials Science 195 (2021) 110474. doi:https://doi.org/10.1016/j.commatsci.2021.110474.
URL https://www.sciencedirect.com/science/article/pii/S0927025621001993

[7] U. Bhardwaj, A. E. Sand, M. Warrier, Comparison of SIA defect morphologies from different interatomic potentials for collision cascades in w, Modelling and Simulation in Materials Science and Engineering 29 (6) (2021) 065015. doi:10.1088/1361-651x/ac095d.
URL https://doi.org/10.1088/1361-651x/ac095d

[8] C. Domain, C. Becquart, L. Malerba, Simulation of radiation damage in fe alloys: an object kinetic monte carlo approach, Journal of Nuclear Materials 335 (1) (2004) 121 – 145. doi:10.1016/j.jnucmat.2004.07.037.

[9] C. Becquart, N. Mousseau, C. Domain, Kinetic Monte Carlo Simulations of Irradiation Effects, in: Comprehensive Nuclear Materials 2nd edition, Volume 1, Elsevier, 2020, pp. 754–778, mise à jour de l'édition 2019. doi:10.1016/B978-0-12-803581-8.11685-6.

[10] W. Setyawan, G. Nandipati, K. J. Roche, H. L. Heinisch, B. D. Wirth, R. J. Kurtz, Displacement cascades and defects annealing in tungsten, part i: Defect database from molecular dynamics simulations, Journal of Nuclear Materials 462 (2015) 329 – 337. doi:10.1016/j.jnucmat.2014.12.056.

[11] A. E. Sand, S. L. Dudarev, K. Nordlund, High-energy collision cascades in tungsten: Dislocation loops structure and clustering scaling laws, EPL (Europhysics Letters) 103 (4) (2013) 46003. doi:10.1209/0295-5075/103/46003.

[12] X. Yi, M. Jenkins, M. Briceno, S. Roberts, Z. Zhou, M. Kirk, In situ study of self-ion irradiation damage in w and w–5re at 500c, Philosophical Magazine 93 (14) (2013) 1715–1738. doi:10.1080/14786435.2012.754110.

[13] X. Yi, A. E. Sand, D. R. Mason, M. A. Kirk, S. G. Roberts, K. Nordlund, S. L. Dudarev, Direct observation of size scaling and elastic interaction between nano-scale defects in collision cascades, EPL 110 (3) (2015) 36001.

[14] M. Dürrschnabel, M. Klimenkov, U. Jäntsch, M. Rieth, H. Schneider, D. Terentyev, New insights into microstructure of neutron-irradiated tungsten, Scientific Reports 11 (1) (2021) 1–17.

[15] E. Little, R. Bullough, M. Wood, On the swelling resistance of ferritic steel, Proceedings of the Royal Society of London. A. Mathematical and Physical Sciences 372 (1751) (1980) 565–579.

[16] F. Gao, D. Bacon, Y. Osetsky, P. Flewitt, T. Lewis, Properties and evolution of sessile interstitial clusters produced by displacement cascades in alpha-iron, Journal of Nuclear Materials 276 (1) (2000) 213 – 220. doi:10.1016/S0022-3115(99)00180-4.

[17] G. Bonny, N. Castin, A. Bakaev, A. Sand, D. Terentyev, Effects of cascade-induced dislocation structures on the long-term microstructural evolution in tungsten, Computational Materials Science 181 (2020) 109727. doi:https://doi.org/10.1016/j.commatsci.2020.109727.

[18] B. L. Eyre, R. Bullough, On the formation of interstitial loops in b.c.c. metals, The Philosophical Magazine: A Journal of Theoretical Experimental and Applied Physics 12 (115) (1965) 31–39. doi:10.1080/14786436508224943.

[19] S. L. Dudarev†, Coherent motion of interstitial defects in a crystalline material, Philosophical Magazine 83 (31-34) (2003) 3577–3597. doi:10.1080/14786430310001599388.

[20] M. W. Finnis, J. E. Sinclair, A simple empirical n-body potential for transition metals, Philosophical Magazine A 50 (1) (1984) 45–55. doi:10.1080/01418618408244210.

[21] N. Juslin, B. Wirth, Interatomic potentials for simulation of he bubble formation in w, Journal of Nuclear Materials 432 (1) (2013) 61 – 66. doi:10.1016/j.jnucmat.2012.07.023.

[22] P. M. Derlet, D. Nguyen-Manh, S. L. Dudarev, Multiscale modeling of crowdion and vacancy defects in body-centered-cubic transition metals, Phys. Rev. B 76 (2007) 054107. doi:10.1103/PhysRevB.76.054107.

[23] C. Björkas, K. Nordlund, S. Dudarev, Modelling radiation effects using the ab-initio based tungsten and vanadium potentials, Nuclear Instruments and Methods in Physics Research Section B: Beam Interactions with Materials and Atoms 267 (18) (2009) 3204 – 3208, proceedings of the Ninth International Conference on Computer Simulation of Radiation Effects in Solids. doi:10.1016/j.nimb.2009.06.123.

[24] M.-C. Marinica, L. Ventelon, M. R. Gilbert, L. Proville, S. L. Dudarev, J. Marian, G. Bencteux, F. Willaime, Interatomic potentials for modelling radiation defects and dislocations in tungsten, Journal of Physics: Condensed Matter 25 (39) (2013) 395502. doi:10.1088/0953-8984/25/39/395502.

[25] A. Sand, J. Dequeker, C. Becquart, C. Domain, K. Nordlund, Non-equilibrium properties of interatomic potentials in cascade simulations in tungsten, Journal of Nuclear Materials 470 (2016) 119 – 127. doi:https://doi.org/10.1016/j.jnucmat.2015.12.012.

[26] S. Plimpton, Fast parallel algorithms for short-range molecular dynamics, J. Comp. Phys. 117 (1995) 1–19.

[27] U. Bhardwaj, H. Hemani, M. Warrier, N. Semwal, K. Ali, A. Arya, Csaransh: Software suite to study molecular dynamics simulations of collision cascades, Journal of Open Source Software (Sep 2019). doi:10.21105/joss.01461.

[28] X. Yi, M. L. Jenkins, M. A. Kirk, Z. Zhou, S. G. Roberts, In-situ tem studies of 150 kev w+ ion irradiated w and w-alloys: Damage production and microstructural evolution, Acta Materialia 112 (2016) 105–120. doi:https://doi.org/10.1016/j.actamat.2016.03.051.
URL https://www.sciencedirect.com/science/article/pii/S135964541630204X

[29] Y. Chen, Y.-H. Li, N. Gao, H.-B. Zhou, W. Hu, G.-H. Lu, F. Gao, H. Deng, New interatomic potentials of w, re and w-re alloy for radiation defects, Journal of Nuclear Materials 502 (2018) 141–153. doi:https://doi.org/10.1016/j.jnucmat.2018.01.059.
URL https://www.sciencedirect.com/science/article/pii/S0022311517313417